

# Noncoplanar magnetic order in the breathing kagome lattice compound $\text{Pb}(\text{OF})\text{Cu}_3(\text{SeO}_3)_2(\text{NO}_3)$

Yimeng Gu<sup>1,2,\*</sup>, Zeyu Kao<sup>1,2,\*</sup>, Yiqing Hao<sup>3,\*</sup>, Weiqin Zhu<sup>1,2</sup>, Qiang Zhang<sup>3</sup>, Yan Wu<sup>3</sup>,  
Changsong Xu<sup>1,2</sup>, Huibo Cao<sup>3</sup> and Jun Zhao<sup>1,2,4,5,6,†</sup>

<sup>1</sup>State Key Laboratory of Surface Physics and Department of Physics, Fudan University, Shanghai 200433, China

<sup>2</sup>Shanghai Qi Zhi Institute, Shanghai 200230, China

<sup>3</sup>Neutron Scattering Division, Oak Ridge National Laboratory, Oak Ridge, Tennessee 37831, USA

<sup>4</sup>Institute of Nanoelectronics and Quantum Computing, Fudan University, Shanghai 200433, China

<sup>5</sup>Shanghai Research Center for Quantum Sciences, Shanghai 201315, China

<sup>6</sup>Collaborative Innovation Center of Advanced Microstructures, Nanjing 210093, China

 (Received 25 June 2023; revised 26 October 2023; accepted 5 December 2023; published 2 January 2024)

We report a comprehensive study investigating the magnetic ordering properties of the quasi-two-dimensional breathing kagome lattice compound  $\text{Pb}(\text{OF})\text{Cu}_3(\text{SeO}_3)_2(\text{NO}_3)$  using neutron diffraction and thermodynamic measurements. A long-range magnetic order emerges below the Néel temperature,  $T_N = 18$  K, characterized by a propagating vector  $\mathbf{k} = (0, 0, 1.5)$ . Refinement analysis reveals that the copper moments display a noncoplanar arrangement, with the  $c$  components parallelly aligned within the breathing kagome plane and antiparallelly aligned between the layers. In-plane moment components form a chiral “tail-chase” structure. The magnetic order is quickly suppressed under moderate external fields applied both within and perpendicular to the kagome plane. Potential magnetic interactions that may be associated with the noncoplanar chiral magnetic structure are discussed.

DOI: [10.1103/PhysRevB.109.024402](https://doi.org/10.1103/PhysRevB.109.024402)

## I. INTRODUCTION

Kagome lattice materials have recently attracted significant interest across various areas of condensed matter physics. As the line graph of the honeycomb lattice, the kagome lattice provides an ideal platform for exploring topologically non-trivial electronic states [1–3] and magnon excitations [4,5]. The electronic band structure of certain kagome materials exhibits nearly flat bands, which can lead to strong electronic correlations [6,7], spin/charge density waves [8–11], and superconductivity [12–14]. Furthermore, the corner-sharing triangular structure of the kagome lattice renders it a highly geometrically frustrated system, potentially giving rise to exotic magnetic states and phases such as spin liquids and spin ices [15–18].

The newly synthesized quasi-two-dimensional magnet  $\text{Pb}(\text{OF})\text{Cu}_3(\text{SeO}_3)_2(\text{NO}_3)$  features a distorted kagome lattice. Copper ions in each layer form a unique motif referred to as the breathing kagome lattice, characterized by alternating bond lengths of 3.205 and 3.492 Å in the corner-sharing triangles. Lead ions separate the breathing kagome layers, yielding a quasi-two-dimensional structure [19]. This breathing structure offers a unique way of tuning the magnetic interactions of the kagome lattice. Previous thermodynamic investigations of polycrystalline samples have indicated the presence of magnetic ordering at temperatures below 18 K. However, to date, there have been no microscopic measurements conducted to elucidate the precise magnetic structure and anisotropy of the

observed magnetism. In this paper, we report neutron diffraction and thermodynamic measurements of magnetic ordering properties in  $\text{Pb}(\text{OF})\text{Cu}_3(\text{SeO}_3)_2(\text{NO}_3)$ .

## II. METHODS

The synthesis of  $\text{Pb}(\text{OF})\text{Cu}_3(\text{SeO}_3)_2(\text{NO}_3)$  single crystals was accomplished through a hydrothermal procedure, similar to those reported in previous studies [19]. The process involved mixing 1.5 mmol of  $\text{CuC}_2\text{O}_4$  (98% purity, sourced from Macklin), 0.5 mmol of  $\text{PbO}$  (99.97% purity, sourced from Aladdin), and 1 mmol of  $\text{SeO}_2$  (99.99% purity, sourced from Aladdin) in powdered form. The mixture was then placed into a 25-ml autoclave reactor along with 0.2 ml of  $\text{HNO}_3$ , 0.1 ml of  $\text{HF}$ , and 2 ml of  $\text{H}_2\text{O}$ . The reactor was heated to 230 °C and maintained at this temperature for 4 days, followed by a gradual cooling to room temperature over an additional 4 days. The resulting brown crystals were washed with distilled water and dried in air. The cleaved surface of the single crystal was determined to be (0,1,2). The sample quality was verified through x-ray diffraction using a high-resolution D8 Discover x-ray diffractometer equipped with a copper x-ray source from Bruker, as shown in Fig. 1.

We have performed heat capacity, susceptibility, and magnetization measurements on single-crystalline  $\text{Pb}(\text{OF})\text{Cu}_3(\text{SeO}_3)_2(\text{NO}_3)$  using the physical property measurement system from Quantum Design. The powder neutron diffraction experiment was carried out on the time-of-flight powder diffractometer, POWGEN, located at the Spallation Neutron Source of the Oak Ridge National Laboratory [20]. The experiment utilized 2.3 grams of powdered sample, which was prepared by grinding single

\*These authors contributed equally to this work.

†Author to whom all correspondence should be addressed: zhaoj@fudan.edu.cn

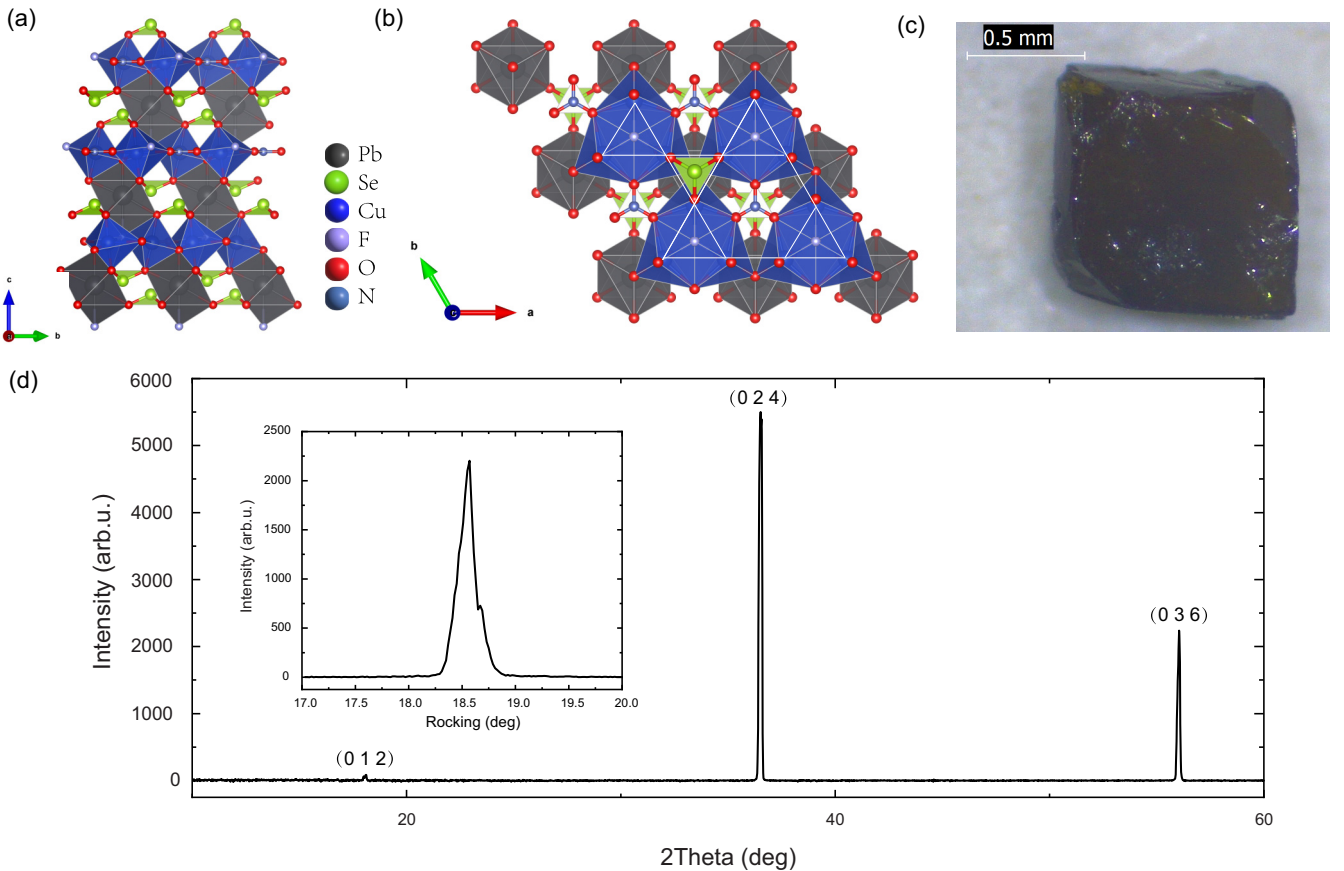


FIG. 1. Crystallographic information of  $\text{Pb(OF)Cu}_3(\text{SeO}_3)_2(\text{NO}_3)$ . (a),(b) Crystal structure has been shown in two different directions. When viewing along the  $a$  axis, a clear quasi-two-dimensional structure could be observed. The breathing kagome lattice could be seen while viewing along the  $c$  axis. The motif has been marked out by white lines. (c) A photograph of a typical  $\text{Pb(OF)Cu}_3(\text{SeO}_3)_2(\text{NO}_3)$  single-crystal sample. (d) The  $\theta$ - $2\theta$  scan of the joint plane  $(0,K,2K)$  of the single-crystal  $\text{Pb(OF)Cu}_3(\text{SeO}_3)_2(\text{NO}_3)$  sample. The inset shows the rocking curve of the  $(0,2,4)$  peak.

crystals. The sample was loaded in a vanadium container and subjected to temperature variations ranging from 5 to 500 K, using a JANIS cryofurnace. Two neutron banks with center wavelengths of 1.5 and 2.665 Å were employed to collect the high-resolution neutron diffraction patterns. The single-crystal neutron diffraction experiment was carried out on Dimensional Extreme Magnetic Neutron Diffractometer, DEMAND, located at the High Flux Isotope Reactor of the Oak Ridge National Laboratory [21]. The wavelength of incident neutron was chosen as 1.5424 Å using the bent Si-220 monochromator. One piece of high-quality single crystal weighing 3.72 mg was used in this experiment and was aligned to the  $(HOL)$  plane. The data reduction used the automated peak search algorithm implemented at DEMAND [22]. The magnetic structure was refined through the Rietveld method using the FULLPROF SUITE software [23]. Symmetry analysis was performed using the SARAH [24] and BILBAO [25,26] programs.

### III. RESULTS AND DISCUSSION

The heat capacity of a single-crystal  $\text{Pb(OF)Cu}_3(\text{SeO}_3)_2(\text{NO}_3)$  sample was measured over a temperature range of 2–30 K, with external magnetic fields

applied both parallel and perpendicular to the breathing kagome plane. As shown in Figs. 2(a) and 2(b), a distinct  $\lambda$ -shaped peak emerges at 18 K in zero field, signaling the onset of a magnetic phase transition, which is in agreement with previous results obtained from powder samples [19]. Under an in-plane magnetic field, the sharp peak in heat capacity shifts to lower temperatures and nearly vanishes at 4 T. When the magnetic field is oriented along the  $c$  axis, the sharp heat capacity anomaly evolves into a broad hump at 0.8 T and disappears at higher fields.

The susceptibility measurements under magnetic fields applied both parallel and perpendicular to the breathing kagome plane are shown in Figs. 3(a) and 3(b). The measurements were taken at 500 Oe for both magnetic field directions. No splitting was observed between zero-field-cooling and field-cooling magnetic susceptibility for both field directions. The susceptibility above 100 K can be fitted by the Curie-Weiss law

$$\chi = \chi_0 + \frac{C}{T - \theta_{\text{CW}}},$$

yielding Curie-Weiss temperatures of  $\theta_{\text{CW}} = 53.0$  K for in-plane magnetic field and  $\theta_{\text{CW}} = 52.4$  K for magnetic field out of the plane. These values are lower than the  $\theta_{\text{CW}} = 66.6$  K

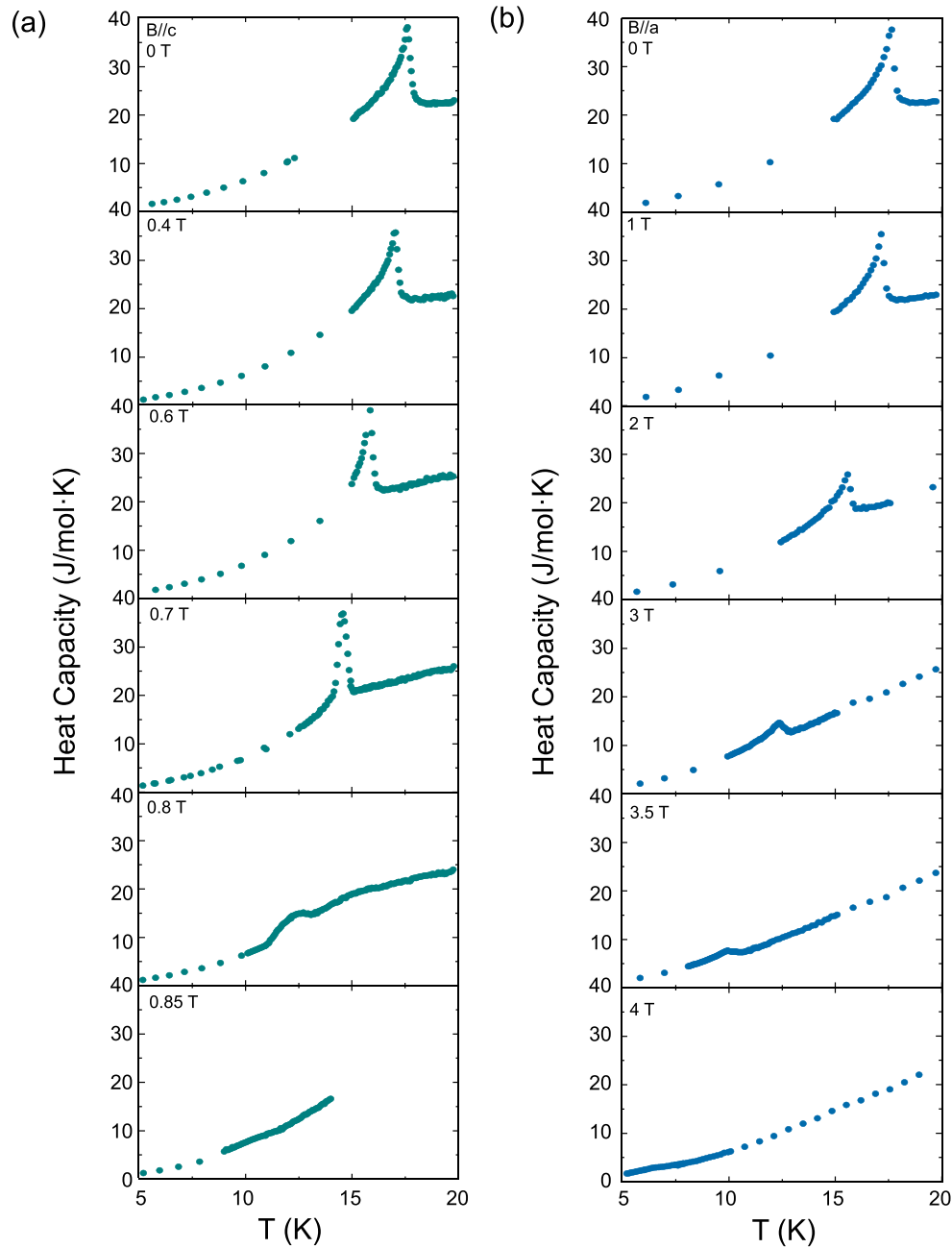


FIG. 2. Heat capacity measured on single-crystal samples of  $\text{Pb}(\text{OF})\text{Cu}_3(\text{SeO}_3)_2(\text{NO}_3)$ . External fields were applied along the  $c$  axis (a) and within the  $ab$  plane (b). The shift of the peak to lower temperature under larger external field could be clearly seen under both field directions. For a magnetic field along the  $c$  axis, the sharp  $\lambda$ -shaped peak evolves into a broad hump at 0.8 T before vanishing under higher field.

determined from a powder sample in previous reports [19]. The positive Curie-Weiss temperature indicates dominant ferromagnetic interactions in  $\text{Pb}(\text{OF})\text{Cu}_3(\text{SeO}_3)_2(\text{NO}_3)$ . The fitted Curie-Weiss constants,  $C$ , are  $16.1510 \times 10^{-6} \text{m}^3 \text{K mol}^{-1}$  and  $14.47 \times 10^{-6} \text{m}^3 \text{K mol}^{-1}$  for magnetic fields along the  $c$  axis and  $ab$  plane, respectively. Effective moments can be calculated from the formula  $\mu_{\text{eff}} = 800 \sqrt{\frac{1}{n} * C}$  [SI], where  $C$  is the Curie-Weiss constant in the International System of Units and  $n$  is the number of magnetic ions in one formula unit. Given the Curie-Weiss constants determined from the

fitting and the three copper ions in one unit cell, the effective moments for the two magnetic field directions are calculated as  $1.856 \mu_B$  and  $1.757 \mu_B$ , respectively.

The magnetization versus external field was measured under two magnetic field directions, as illustrated in the main panels of Figs. 3(c) and 3(d). As the magnetic field within the kagome plane increases, the magnetization at 2 K rises linearly, reaching saturation at approximately 5 T. This suggests that the magnetic moments progressively rotate from the  $c$  axis toward the kagome plane. In contrast, a sudden increase in magnetization occurs at 0.9 T when the magnetic field is

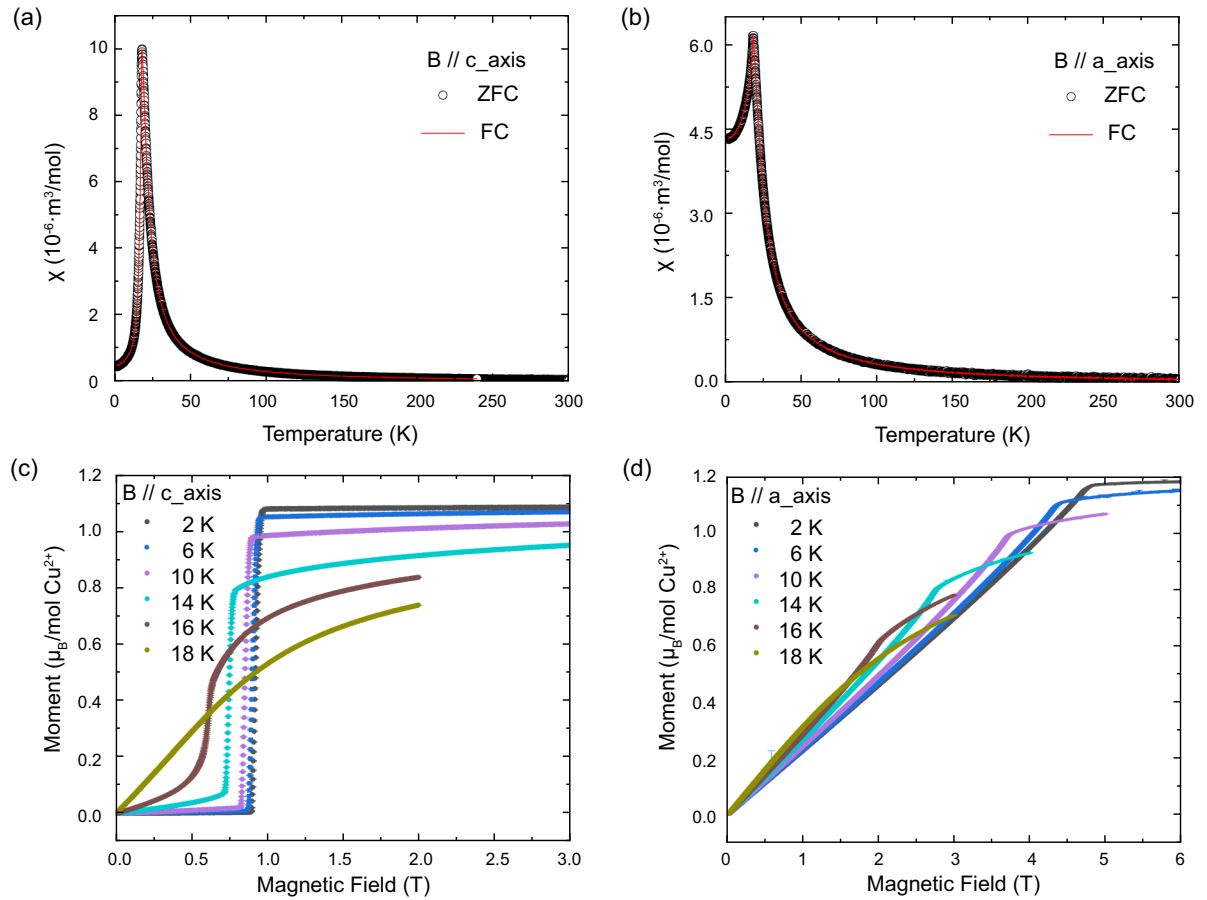


FIG. 3. Magnetization along with susceptibility measured on single-crystalline  $\text{Pb}(\text{OF})\text{Cu}_3(\text{SeO}_3)_2(\text{NO}_3)$  samples. Measurements were taken under magnetic field along both the  $c$  axis and the  $a$  axis. As shown in panels (a) and (b), the field-cooling and zero-field-cooling curves show no splitting for both field directions. The high-temperature behavior of susceptibility follows the Curie-Weiss law. Magnetization curves for both field directions are shown in panels (c) and (d). When an in-plane field is applied, the moments gradually become polarized with increasing magnetic field. However, when a  $c$ -axis field is applied, the moments are abruptly polarized at 0.9 T. The fully polarized moment for  $\text{Pb}(\text{OF})\text{Cu}_3(\text{SeO}_3)_2(\text{NO}_3)$  is about  $1\mu_B$  for both field directions.

applied parallel to the  $c$  axis, signifying a first-order spin-flip transition. This might be due to an abrupt flip of one sublattice magnetization within the antiferromagnetic order to align with the field. With increasing temperature, the saturation fields gradually decrease for both field directions. The phase diagrams for both field orientations are summarized Figs. 4(a) and 4(b).

To further examine the lattice and magnetic structure of  $\text{Pb}(\text{OF})\text{Cu}_3(\text{SeO}_3)_2(\text{NO}_3)$ , we conducted a neutron diffraction experiment on a polycrystalline sample obtained by grinding single crystals of this compound at POWGEN. Refinements reveal that the crystal structure undergoes minimal change during cooling. Refined crystal structure parameters are provided in Table I. Upon cooling to 5 K below the phase transition temperature, additional peaks emerge in the diffraction patterns, which can be indexed by the magnetic propagation vector  $\mathbf{k} = (0, 0, 1.5)$ . The intensity of peak (0,1,0.5) as a function of temperature, shown in Fig. 5(c), indicates the onset of long-range magnetic order at 18.26 K, aligning with the heat capacity and susceptibility measurements.

The magnetic structure models of  $\text{Pb}(\text{OF})\text{Cu}_3(\text{SeO}_3)_2(\text{NO}_3)$  were determined with the

assistance of the Bilbao Crystallographic Server [25,26]. The maximal magnetic space groups for the space group  $R\bar{3}m$  with a propagation vector  $\mathbf{k} = (0, 0, 1.5)$  are  $R_73c$  (#161.72) and  $R_73m$  (#160.68), resulting in a group-subgroup index of 2. The magnetic structures derived from these two magnetic space groups take the form of  $[M_x, -M_x, M_z]$  and  $[M_x, M_x, 0]$ , respectively. Refinement based on the first model reveals a magnetic structure with moments predominantly aligned in the  $c$  direction, exhibiting a slight canting of less than 5% of the total ordered moment, which we refer to as the “collinear” structure in subsequent discussions. The second model yields a purely in-plane structure where moments are aligned  $120^\circ$  apart from each other, denoted as the “120-degree” structure herein. The illustration of these two magnetic structure models is shown in Figs. 7(c) and 7(d). However, neither model adequately accounts for the observed peak intensity.

Improved results can be achieved by using the magnetic space group  $R_73$  (#146.12) with a group-subgroup index of 4. This magnetic space group can be understood as a combination of the two maximal subgroups, yielding a canted structure in which the  $c$ -axis components are aligned antiparallel to each other, and the in-plane portion forms a local chiral

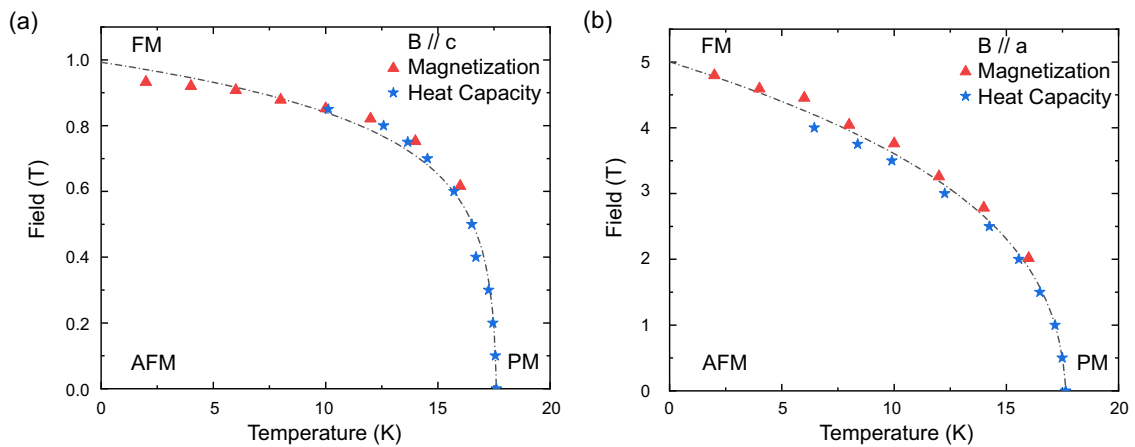


FIG. 4. Phase diagram of  $\text{Pb(OF)Cu}_3(\text{SeO}_3)_2(\text{NO}_3)$  under two different field directions. The data points are collected from magnetization and heat capacity measurements. The critical field for the magnetic field along the  $c$  direction is slightly smaller than 1 T in contrast to a 5-T critical field for the in-plane field.

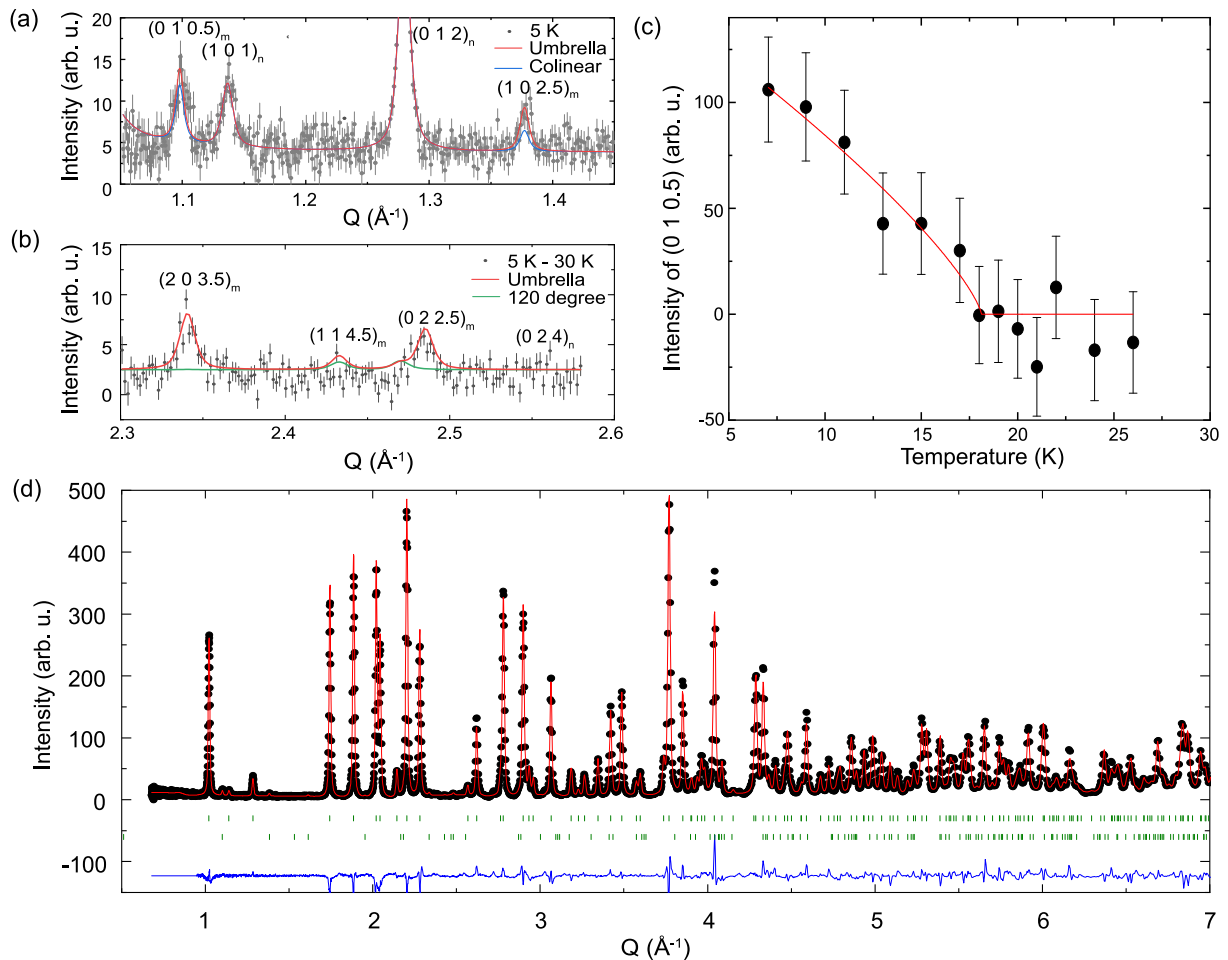


FIG. 5. Neutron diffraction taken on polycrystalline  $\text{Pb(OF)Cu}_3(\text{SeO}_3)_2(\text{NO}_3)$  at POWGEN, SNS. Comparison among the refinement according to the three magnetic structure models are demonstrated in panels (a) and (b). (c) The intensity of the magnetic peak (0,1,0.5) behaves as an order parameter of the antiferromagnetic phase transition in  $\text{Pb(OF)Cu}_3(\text{SeO}_3)_2(\text{NO}_3)$  with a phase transition temperature  $T_N = 18.26$  K. (d) The full pattern of the neutron diffraction of  $\text{Pb(OF)Cu}_3(\text{SeO}_3)_2(\text{NO}_3)$  measured at 5 K with refinement under the umbrella spin structure model with a magnetic  $R$  factor of  $R_f = 0.034$ . Black dots stand for data points while red lines are from Rietveld refinements. The blue line indicates the difference between refinement and data.

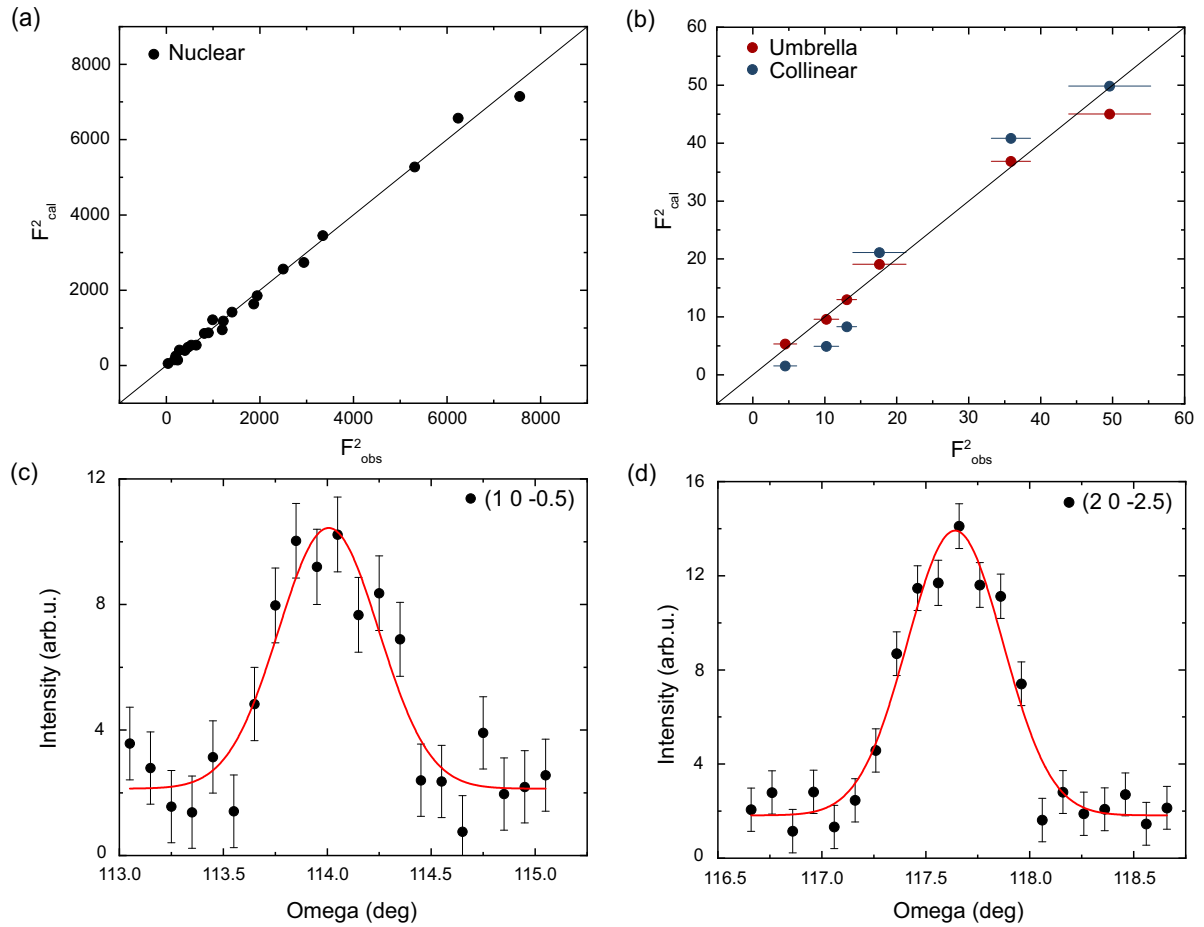


FIG. 6. Neutron diffraction taken on single-crystalline  $\text{Pb}(\text{OF})\text{Cu}_3(\text{SeO}_3)_2(\text{NO}_3)$  at DEMAND, HFIR. The integrated intensity of nuclear Bragg peaks shown in panel (a) give satisfying agreement with the crystal structure proposed in previous research [19]. The comparison between two magnetic structure candidates given by powder neutron diffraction is shown in panel (b). Panels (c) and (d) show typical magnetic Bragg peaks observed in the single-crystal neutron diffraction experiment. The data was measured at 5 K. A half- $\lambda$  background measured at 25 K has been subtracted from the data.

structure. We refer to this model as the “umbrella” structure in the following discussion.

Refinement using the umbrella structural model demonstrates reasonably good agreement with our powder neutron diffraction dataset, yielding overall  $R$  factors of  $R_p = 0.093$  and  $R_{wp} = 0.098$  with a  $\chi^2$  of 16.7. The comparison between the refinements of the three potential models is illustrated in Figs. 5(a) and 5(b). The umbrella structure successfully reproduces the correct peak intensity, while the collinear model yields a smaller peak height than the data for both magnetic peaks at  $(0,1,0.5)$  and  $(1,0,2.5)$ . The 120-degree model fails to account for a strong magnetic peak at  $(2,0,3.5)$ . Figure 5(d) displays the full pattern of refinement using the umbrella model. The in-plane part of the magnetic moments is projected onto  $[M_x, M_x]$  and  $[-M_x, M_x]$  directions in the refinement, which are two orthogonal directions within the breathing kagome plane. According to our original refinement, the  $[-M_x, M_x]$  component is only  $-0.06(15)\mu_B$ , which is close to zero within uncertainty so it is set to zero in our further analysis. The  $c$  component is parallel within the breathing kagome plane and antiparallel between adjacent kagome planes. The in-plane portion adopts a 120-degree

structure for every corner-sharing triangle in the breathing kagome motif, forming a local chiral structure in which triangles sharing the same corner exhibit opposite chirality. The refined ordered moment for copper ions is approximately  $0.81(6)\mu_B$  per copper ion, with an in-plane part of  $0.32(7)\mu_B$  and an out-of-plane component of  $0.74(6)\mu_B$  and is smaller than the expected value for a spin-1/2 system with a  $g$  factor of 2.16.

When considering the small in-plane part obtained from the powder neutron diffraction experiment, it is evident that it closely approaches the resolution limit of  $\sim 0.2\mu_B$  at POWGEN. Therefore, we performed further neutron diffraction experiments on a single-crystalline  $\text{Pb}(\text{OF})\text{Cu}_3(\text{SeO}_3)_2(\text{NO}_3)$  at DEMAND. In our refinement process, we incorporated 23 nuclear Bragg peaks and 6 magnetic Bragg peaks. The crystal structure model was constrained to align with the findings derived from our powder neutron diffraction results, with the exception of the atom displacement factors, which were subject to refinement. During the magnetic structure refinement, we fixed all structural parameters while allowing for the adjustment of magnetic moments. The nuclear peaks collected in the experiment show satisfying consistency with

TABLE I. Crystallographic and magnetic structure parameters obtained from neutron diffraction.

| Crystal structure    |                   |                        |                   |                              |
|----------------------|-------------------|------------------------|-------------------|------------------------------|
| $a$                  | $b$               | $c$                    |                   |                              |
| 6.665 Å              | 6.665 Å           | 18.448 Å               |                   |                              |
| $\alpha$             | $\beta$           | $\gamma$               |                   |                              |
| 90°                  | 90°               | 120°                   |                   |                              |
| Space group          |                   |                        |                   |                              |
| $R3m$ (No. 160)      |                   |                        |                   |                              |
| Atom position        |                   |                        |                   |                              |
| Atom                 | $x$               | $y$                    | $z$               | $B$ factor (Å <sup>2</sup> ) |
| Pb                   | 0.6667            | 0.3333                 | 0.3421(3)         | 0.27(4)                      |
| Se1                  | 0.3333            | 0.6667                 | 0.3583(3)         | 0.48(7)                      |
| Se2                  | 0.6667            | 0.3333                 | 0.6424(3)         | 0.48(7)                      |
| Cu                   | 0.5076(2)         | 0.4924(2)              | 0.5000            | 0.03(2)                      |
| F                    | 0.3333            | 0.6667                 | 0.5244(4)         | 0.30(9)                      |
| O1                   | 0.6667            | 0.3333                 | 0.4723(4)         | 0.37(9)                      |
| O2                   | 0.4647(4)         | 0.5353(4)              | 0.3978(3)         | 0.37(9)                      |
| O3                   | 0.5343(3)         | 0.4657(3)              | 0.6037(3)         | 0.37(9)                      |
| O4                   | 0.1063(5)         | 0.2126(11)             | 0.5047(3)         | 0.37(9)                      |
| N                    | 0.0000            | 0.0000                 | 0.5055(3)         | 0.35(4)                      |
| Magnetic structure   |                   |                        |                   |                              |
| Magnetic space group |                   |                        |                   |                              |
| $R_73$ (#146.12)     |                   |                        |                   |                              |
| Moment               |                   |                        |                   |                              |
| Cu                   | $ M_{11} $        | $ M_{\bar{1}\bar{1}} $ | $ M_c $           | $ M_{\text{tot}} $           |
|                      | 0.361(34) $\mu_B$ | 0.00 $\mu_B$           | 0.826(25) $\mu_B$ | 0.901(22) $\mu_B$            |

the proposed crystal structure [19], giving an  $R$  factor of  $R_f = 0.041$ . The refinement is shown in Fig. 6(a). No Bragg peaks were observed in the symmetry-forbidden  $L$  zone, proving that our sample is single domain. A series of magnetic peaks in the  $(HOL)$  plane could be observed clearly as well. We tried both collinear and umbrella magnetic structure models under fixed crystal structure parameters to fit the magnetic peaks. The umbrella structure gives much better fitting results with a magnetic  $R$  factor of  $R_f = 0.034$  compared to a magnetic  $R$  factor of  $R_f = 0.129$  given by the collinear structure. The fitting results are shown in Fig. 6(b). These results further confirm the existence of nonzero in-plane magnetic moments in  $\text{Pb}(\text{OF})\text{Cu}_3(\text{SeO}_3)_2(\text{NO}_3)$ . The refined ordered moment we got from our single-crystal neutron diffraction experiment is  $0.36(3)\mu_B/\text{Cu}^{2+}$  along the  $[110]$  direction and  $0.82(3)\mu_B/\text{Cu}^{2+}$  along the  $c$  axis, consistent with the results in powder diffraction. The total moment  $0.90(2)\mu_B/\text{Cu}^{2+}$  is closer to the saturation moment of our magnetization curves. Table I offers detailed information on the magnetic moments. The comparison between the observed magnetic structure factors and the calculated magnetic structure factors for the magnetic peaks within the  $(HOL)$  plane according to both magnetic structure models could be found in Table II. The illustration of the noncoplanar magnetic structure is shown in Figs. 7(a) and 7(b).

We note that the  $c$  components of the moments exhibit parallel alignment within the breathing kagome plane, but antiparallel alignment between the breathing kagome layers. This seems consistent with susceptibility measurements that reveal a positive Curie-Weiss temperature. The magnetic structure of  $\text{Pb}(\text{OF})\text{Cu}_3(\text{SeO}_3)_2(\text{NO}_3)$  is more complicated than the widely studied  $\text{Cu}(1,3\text{-bdc})$  and

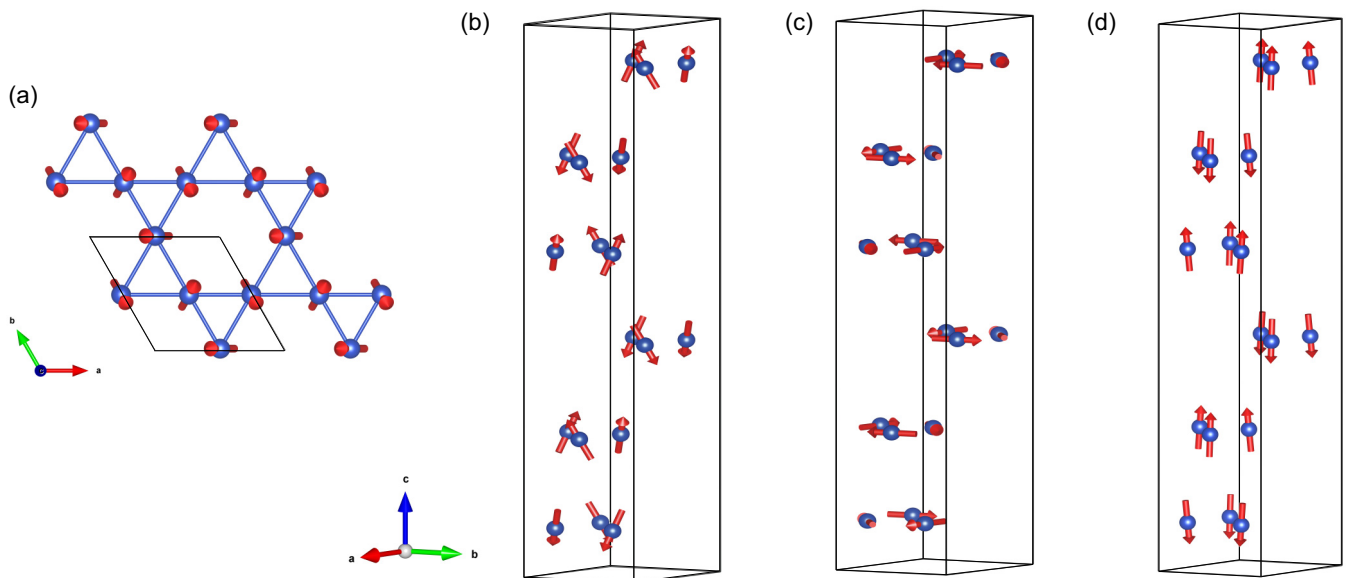


FIG. 7. Magnetic structure of  $\text{Pb}(\text{OF})\text{Cu}_3(\text{SeO}_3)_2(\text{NO}_3)$ . In (a), we provide an enlarged view of the in-plane magnetic arrangement, where the moments lie along the  $(HH)$  and symmetric directions. This configuration forms a local 120-degree chiral structure, wherein triangles sharing the same corner exhibit opposite chirality, referred to as the tail-chase geometry. In (b), we present a comprehensive diagram of the magnetic structure of  $\text{Pb}(\text{OF})\text{Cu}_3(\text{SeO}_3)_2(\text{NO}_3)$ , obtained through Rietveld refinement. Here, the magnetic moments are canted toward the  $ab$  plane. Our refinement indicates an ordered moment of  $0.90(2)\mu_B$  for each individual copper ion. Panel (c) shows the 120-degree structure in correspondence with the magnetic space group  $R_73m$  (#160.68), while panel (d) depicts the collinear structure model under the magnetic space group  $R_73c$  (#161.72). The models depicted in (c) and (d) are unable to fully explain our experimental data.

TABLE II. Comparison between observed magnetic structure factors and calculated magnetic structure factors given by umbrella and collinear magnetic structures. The error bar of the integrated peak intensities is given in the parentheses.

| $Q$        | F2obs        | F2cal_umbrella | F2cal_collinear |
|------------|--------------|----------------|-----------------|
| (1 0 -0.5) | 13.05 (1.38) | 13.00          | 8.33            |
| (1 0 2.5)  | 10.22 (1.72) | 9.59           | 4.95            |
| (1 0 5.5)  | 4.50 (1.59)  | 5.34           | 1.55            |
| (2 0 0.5)  | 49.59 (5.70) | 45.02          | 49.86           |
| (2 0 -2.5) | 35.87 (2.73) | 36.88          | 40.83           |
| (2 0 -5.5) | 17.59 (3.70) | 19.11          | 21.13           |

V-jarosite  $\text{KV}_3(\text{OH})_6(\text{SO}_4)_2$  in which the magnetic moments are aligned ferromagnetically within the kagome plane and antiferromagnetically between adjacent planes [4,27–29]. The tail-chase-like in-plane structure could be regarded as a periodic arrangement of toroidal moments which violates space inversion and time reversal symmetry [30,31] and could introduce ferrotoroidicity, which is regarded as the fourth primary ferroic order [30].

The formation of the in-plane noncollinear tail-chase magnetic structure in  $\text{Pb}(\text{OF})\text{Cu}_3(\text{SeO}_3)_2(\text{NO}_3)$  can potentially be attributed to the interplay of various factors. One such factor is dipole-dipole interactions, which could influence the alignment and arrangement of the magnetic moments, contributing to the observed magnetic structure [32]. Furthermore, the involvement of further-neighbor exchange interactions could also play a role in shaping the magnetic structure [33–36]. Additionally, the absence of inversion symmetry in the breathing kagome lattice could give rise to Dzyaloshinsky-Moriya (DM) interactions. These interactions result from the relativistic spin-orbit coupling and tend to favor non-collinear or chiral magnetic configurations [37–40]. To gain a more precise understanding of the magnetic interactions in  $\text{Pb}(\text{OF})\text{Cu}_3(\text{SeO}_3)_2(\text{NO}_3)$ , further investigations into spin dynamics using inelastic neutron scattering are considered essential.

## IV. CONCLUSION

In summary, we have successfully synthesized high-quality single crystals of the breathing kagome lattice magnet  $\text{Pb}(\text{OF})\text{Cu}_3(\text{SeO}_3)_2(\text{NO}_3)$ . We measured its heat capacity and magnetic susceptibility, finding a phase transition at 18 K that can be suppressed by moderate external magnetic fields applied both within and perpendicular to the kagome plane. To unravel the magnetic structure of  $\text{Pb}(\text{OF})\text{Cu}_3(\text{SeO}_3)_2(\text{NO}_3)$ , we have performed neutron diffraction experiments on both polycrystalline and single-crystalline samples, allowing us to determine the magnetic structure in the absence of an applied magnetic field. Our results indicate that the copper moments form a noncoplanar magnetic structure, with the  $c$  components parallelly aligned within the breathing kagome plane and antiparallelly aligned between the layers. The in-plane components of the moments exhibit a chiral tail-chase structure. This unique magnetic structure could be driven by interactions beyond the nearest-neighbor Heisenberg interactions, such as DM interactions, dipole-dipole interactions, and further-neighbor interactions. To fully understand the magnetic interactions governing this system, further investigations employing inelastic neutron scattering techniques and theoretical calculations are necessary. Our findings contribute to expanding knowledge of kagome lattice materials and provide a solid foundation for future studies exploring the exotic magnetic properties and potential applications of these systems.

## ACKNOWLEDGMENTS

We thank Z. Z. He for helpful discussions. This work was supported by the National Key R&D Program of China (2022YFA1403202), Key Program of National Natural Science Foundation of China (Grant No. 12234006), and the Shanghai Municipal Science and Technology Major Project (Grant No. 2019SHZDZX01). This research used resources at the High Flux Isotope Reactor and Spallation Neutron Source, DOE Office of Science User Facilities operated by the Oak Ridge National Laboratory.

- [1] A. Mielke, Ferromagnetism in the Hubbard model on line graphs and further considerations, *J. Phys. A: Math. Gen.* **24**, 3311 (1991).
- [2] Z. Liu, F. Liu, and Y.-S. Wu, Exotic electronic states in the world of flat bands: From theory to material, *Chin. Phys. B* **23**, 077308 (2014).
- [3] E. J. Bergholtz and Z. Liu, Topological flat band models and fractional Chern insulators, *Int. J. Mod. Phys. B* **27**, 1330017 (2013).
- [4] R. Chisnell, J. S. Helton, D. E. Freedman, D. K. Singh, R. I. Bewley, D. G. Nocera, and Y. S. Lee, Topological magnon bands in a kagome lattice ferromagnet, *Phys. Rev. Lett.* **115**, 147201 (2015).
- [5] A. Mook, J. Henk, and I. Mertig, Magnon Hall effect and topology in kagome lattices: A theoretical investigation, *Phys. Rev. B* **89**, 134409 (2014).
- [6] M. Kang, L. Ye, S. Fang, J. S. You, A. Levitan, M. Han, J. I. Facio, C. Jozwiak, A. Bostwick, E. Rotenberg, M. K. Chan, R. D. McDonald, D. Graf, K. Kaznatcheev, E. Vescovo, D. C. Bell, E. Kaxiras, J. van den Brink, M. Richter, M. Prasad Ghimire, J. G. Checkelsky, and R. Comin, Dirac fermions and flat bands in the ideal kagome metal  $\text{FeSn}$ , *Nat. Mater.* **19**, 163 (2020).
- [7] M. Kang, S. Fang, L. Ye, H. C. Po, J. Denlinger, C. Jozwiak, A. Bostwick, E. Rotenberg, E. Kaxiras, J. G. Checkelsky, and R. Comin, Topological flat bands in frustrated kagome lattice  $\text{CoSn}$ , *Nat. Commun.* **11**, 4004 (2020).
- [8] H. W. S. Arachchige, W. R. Meier, M. Marshall, T. Matsuoka, R. Xue, M. A. McGuire, R. P. Hermann, H. Cao, and D. Mandrus, Charge density wave in kagome lattice intermetallic  $\text{ScV}_6\text{Sn}_6$ , *Phys. Rev. Lett.* **129**, 216402 (2022).
- [9] G. Ding, H. Wo, Y. Gu, Y. Gu, and J. Zhao, Effect of chromium doping on superconductivity and charge density wave order in the kagome metal  $\text{Cs}(\text{V}_{1-x}\text{Cr}_x)_3\text{Sb}_5$ , *Phys. Rev. B* **106**, 235151 (2022).
- [10] X. Teng, J. S. Oh, H. Tan, L. Chen, J. Huang, B. Gao, J.-X. Yin, J.-H. Chu, M. Hashimoto, D. Lu, C. Jozwiak, A. Bostwick, E.

- Rotenberg, G. E. Granroth, B. Yan, R. J. Birgeneau, P. Dai, and M. Yi, Magnetism and charge density wave order in kagome FeGe, *Nat. Phys.* **19**, 814 (2023).
- [11] S.-L. Yu and J.-X. Li, Chiral superconducting phase and chiral spin-density-wave phase in a Hubbard model on the kagome lattice, *Phys. Rev. B* **85**, 144402 (2012).
- [12] B. R. Ortiz, S. M. L. Teicher, Y. Hu, J. L. Zuo, P. M. Sarte, E. C. Schueller, A. M. M. Abeykoon, M. J. Krogstad, S. Rosenkranz, R. Osborn, R. Seshadri, L. Balents, J. He, and S. D. Wilson, CsV<sub>3</sub>Sb<sub>5</sub>: A Z<sub>2</sub> topological kagome metal with a superconducting ground state, *Phys. Rev. Lett.* **125**, 247002 (2020).
- [13] H. Zhao, H. Li, B. R. Ortiz, S. M. L. Teicher, T. Park, M. Ye, Z. Wang, L. Balents, S. D. Wilson, and I. Zeljkovic, Cascade of correlated electron states in the kagome superconductor CsV<sub>3</sub>Sb<sub>5</sub>, *Nature (London)* **599**, 216 (2021).
- [14] T. Neupert, M. M. Denner, J.-X. Yin, R. Thomale, and M. Z. Hasan, Charge order and superconductivity in kagome materials, *Nat. Phys.* **18**, 137 (2022).
- [15] T. H. Han, J. S. Helton, S. Chu, D. G. Nocera, J. A. Rodriguez-Rivera, C. Broholm, and Y. S. Lee, Fractionalized excitations in the spin-liquid state of a kagome-lattice antiferromagnet, *Nature (London)* **492**, 406 (2012).
- [16] E. Mengotti, L. J. Heyderman, A. F. Rodríguez, F. Nolting, R. V. Hügli, and H.-B. Braun, Real-space observation of emergent magnetic monopoles and associated Dirac strings in artificial kagome spin ice, *Nat. Phys.* **7**, 68 (2011).
- [17] G.-W. Chern and O. Tchernyshyov, Magnetic charge and ordering in kagome spin ice, *Philos. Trans. R. Soc., A* **370**, 5718 (2012).
- [18] S. Yan, D. A. Huse, and S. R. White, Spin-liquid ground state of the  $S = 1/2$  kagome Heisenberg antiferromagnet, *Science* **332**, 1173 (2011).
- [19] M. Zhang, Z. Zhao, W. Zhang, J. Li, X. Huang, and Z. He, Pb(OF)Cu<sub>3</sub>(SeO<sub>3</sub>)<sub>2</sub>(NO<sub>3</sub>): A selenite fluoride nitrate with a breathing kagomé lattice, *Chem. Commun.* **56**, 11965 (2020).
- [20] A. Huq, M. Kirkham, P. F. Peterson, J. P. Hodges, P. S. Whitfield, K. Page, T. Hugle, E. B. Iverson, A. Parizzi, and G. Rennich, POWGEN: Rebuild of a third-generation powder diffractometer at the Spallation Neutron Source, *J. Appl. Crystallogr.* **52**, 1189 (2019).
- [21] H. Cao, B. C. Chakoumakos, K. M. Andrews, Y. Wu, R. A. Riedel, J. Hodges, W. Zhou, R. Gregory, B. Haberl, J. Molaison, and G. W. Lynn, DEMAND, a dimensional extreme magnetic neutron diffractometer at the High Flux Isotope Reactor, *Crystals* **9**, 5 (2019).
- [22] Y. Hao, E. Feng, D. Lu, L. Zimmer, Z. Morgan, B. C. Chakoumakos, G. Zhang, and H. Cao, Machine-learning-assisted automation of single-crystal neutron diffraction, *J. Appl. Crystallogr.* **56**, 519 (2023).
- [23] J. Rodríguez-Carvajal, Recent advances in magnetic structure determination by neutron powder diffraction, *Physica B (Amsterdam, Neth.)* **192**, 55 (1993).
- [24] A. S. Wills, A new protocol for the determination of magnetic structures using simulated annealing and representational analysis (SARAH), *Physica B (Amsterdam, Neth.)* **276-278**, 680 (2000).
- [25] M. I. Aroyo, A. Kirov, C. Capillas, J. M. Perez-Mato, and H. Wondratschek, Bilbao Crystallographic Server. II. Representations of crystallographic point groups and space groups, *Acta Crystallogr., Sect. A: Found. Adv.* **62**, 115 (2006).
- [26] M. I. Aroyo, J. M. Perez-Mato, C. Capillas, E. Kroumova, S. Ivantchev, G. Madariaga, A. Kirov, and H. Wondratschek, Bilbao Crystallographic Server: I. Databases and crystallographic computing programs, *Z. Kristallogr.* **221**, 15 (2006).
- [27] R. Chisnell, J. S. Helton, D. E. Freedman, D. K. Singh, F. Demmel, C. Stock, D. G. Nocera, and Y. S. Lee, Magnetic transitions in the topological magnon insulator Cu(1,3-bdc), *Phys. Rev. B* **93**, 214403 (2016).
- [28] D. Papoutsakis, D. Grohol, and D. G. Nocera, Magnetic properties of a homologous series of vanadium jarosite compounds, *J. Am. Chem. Soc.* **124**, 2647 (2002).
- [29] M. Kato, T. Hori, N. Oba, K. Yoshimura, and T. Goto, Magnetic properties of V-jarosite AV<sub>3</sub>(SO<sub>4</sub>)<sub>2</sub>(OH)<sub>6</sub> (A=Na,K) with kagome lattice, *Physica B (Amsterdam, Neth.)* **329-333**, 1042 (2003).
- [30] C. Ederer and N. A. Spaldin, Towards a microscopic theory of toroidal moments in bulk periodic crystals, *Phys. Rev. B* **76**, 214404 (2007).
- [31] A. A. Gorbatsevich and Y. V. Kopaev, Toroidal order in crystals, *Ferroelectrics* **161**, 321 (1994).
- [32] S. Hayashida, H. Ishikawa, Y. Okamoto, T. Okubo, Z. Hiroi, M. Avdeev, P. Manuel, M. Hagihala, M. Soda, and T. Masuda, Magnetic state selected by magnetic dipole interaction in the kagome antiferromagnet NaBa<sub>2</sub>Mn<sub>3</sub>F<sub>11</sub>, *Phys. Rev. B* **97**, 054411 (2018).
- [33] J. C. Domenge, P. Sindzingre, C. Lhuillier, and L. Pierre, Twelve sublattice ordered phase in the  $J_1$ - $J_2$  model on the kagome lattice, *Phys. Rev. B* **72**, 024433 (2005).
- [34] S.-S. Gong, W. Zhu, L. Balents, and D. N. Sheng, Global phase diagram of competing ordered and quantum spin-liquid phases on the kagome lattice, *Phys. Rev. B* **91**, 075112 (2015).
- [35] H. J. Liao, Z. Y. Xie, J. Chen, Z. Y. Liu, H. D. Xie, R. Z. Huang, B. Normand, and T. Xiang, Gapless spin-liquid ground state in the  $S = 1/2$  kagome antiferromagnet, *Phys. Rev. Lett.* **118**, 137202 (2017).
- [36] A. S. Wills, A. Harrison, C. Ritter, and R. I. Smith, Magnetic properties of pure and diamagnetically doped jarosites: Model kagome antiferromagnets with variable coverage of the magnetic lattice, *Phys. Rev. B* **61**, 6156 (2000).
- [37] T. Arh, M. Gomilšek, P. Prelovšek, M. Pregelj, M. Klanjšek, A. Ozarowski, S. J. Clark, T. Lancaster, W. Sun, J. X. Mi, and A. Zorko, Origin of magnetic ordering in a structurally perfect quantum kagome antiferromagnet, *Phys. Rev. Lett.* **125**, 027203 (2020).
- [38] A. Zorko, M. Pregelj, M. Gomilšek, M. Klanjšek, O. Zaharko, W. Sun, and J. X. Mi, Negative-vector-chirality 120° spin structure in the defect- and distortion-free quantum kagome antiferromagnet YCu<sub>3</sub>(OH)<sub>6</sub>Cl<sub>3</sub>, *Phys. Rev. B* **100**, 144420 (2019).
- [39] K. Matan, D. Grohol, D. G. Nocera, T. Yildirim, A. B. Harris, S. H. Lee, S. E. Nagler, and Y. S. Lee, Spin waves in the frustrated kagomé lattice antiferromagnet KFe<sub>3</sub>(OH)<sub>6</sub>(SO<sub>4</sub>)<sub>2</sub>, *Phys. Rev. Lett.* **96**, 247201 (2006).
- [40] R. Ballou, B. Canals, M. Elhajal, C. Lacroix, and A. Wills, Magnetic ground state of Kagomé systems: The example of the jarosites compounds, *Phys. Status Solidi B* **236**, 240 (2003).